Report: Comparison of Atomic and Electronic Structures of Silica and Sodium Silicate Glasses

N. Adelstein, V. Lordi

November 4, 2014

Disclaimer

This document was prepared as an account of work sponsored by an agency of the United States government. Neither the United States government nor Lawrence Livermore National Security, LLC, nor any of their employees makes any warranty, expressed or implied, or assumes any legal liability or responsibility for the accuracy, completeness, or usefulness of any information, apparatus, product, or process disclosed, or represents that its use would not infringe privately owned rights. Reference herein to any specific commercial product, process, or service by trade name, trademark, manufacturer, or otherwise does not necessarily constitute or imply its endorsement, recommendation, or favoring by the United States government or Lawrence Livermore National Security, LLC. The views and opinions of authors expressed herein do not necessarily state or reflect those of the United States government or Lawrence Livermore National Security, LLC, and shall not be used for advertising or product endorsement purposes.

Report:
Comparison of Atomic and Electronic Structures of Silica and Sodium Silicate Glasses
(Submitted to NNSA WMS Team as deliverable for project LL13-MatModelRadDetect-PD2Jf, PI: Lordi)

N. Adelstein and V. Lordi
Lawrence Livermore National Laboratory
10/06/2014

Introduction

Glass scintillators may hold great promise for low-cost, large-volume, shapeable radiation detectors. However, the light yield and energy resolution of glass scintillators to-date have been more than an order of magnitude worse than for crystalline scintillators and far from the theoretical limits. Glass scintillators are fabricated by dissolving rare-earth dopants into a glass matrix. Their operation relies on gamma ray absorption in the glass generating electrons and holes that must migrate to a rare-earth activator atom to emit light. The transport of carriers in the glass limits the performance, particularly in glasses where the solubility limit of activator is low, since carriers may recombine non-radiatively before reaching an activator atom.

In this work, we aim to use atomistic simulations to discover the nature of electron transport in specific glass materials and how it may be enhanced by tuning the composition or forming process. The analysis proceeds in two steps: generation of a computational model of a given glass's atomic structure, then extraction of the electronic structure to correlate electronic structure with carrier transport. Here we report results for two glasses: silica (SiO_2) and sodium silicate ($Na_2O:SiO_2$). Multiple compositions of the latter are studied, namely $Na_2O:SiO_2$ ratios of of 1:2, 1:3, and 3:7, with most results focused on the 3:7 composition.

The overall goal is to establish a computational framework that can mimic a range of experimental glass structures by tuning computational parameters in the construction of the glass model, and enable studies of the correlation between atomic structure and electronic transport properties of the glass materials. These correlations would direct synthesis parameters for a given glass to optimize its transport properties.

Methods

A variety of ways exist to characterize an amorphous structure and assess its correspondence to experimentally realized glasses, with various degrees of sensitivity of the different measures. One of the simplest measures, the radial distribution function (rdf), is not very sensitive to subtleties in the structure, so additional metrics are needed. Through NMR and neutron diffraction experiments, the number of non-bridging oxygen (nbo) atoms can be determined. In addition, the average number of nbo connected to each Si atom (related to the Q^n number) and the ring structure can also be determined. Various experimental techniques, including X-ray and neutron diffraction, are sensitive to angular distributions, which comprise further comparative metrics for simulated structures.

In simulations, the sample volume is generally small compared to macroscopic experimental samples. Thus, an adequate sampling of the amorphous structure over macroscopic length scales requires averaging the simulations over an ensemble of "snapshots." With molecular dynamics, these snapshots may be obtained by sampling the dynamics periodically, with the period chosen longer than the timescale of dynamic correlations. This relies on the ergodicity principle of the

equivalence of time and spatial averages of the ensemble. The following analyses form a suite of tools to characterize the structure of the glass during the generation procedure.

Structural Parameters

a) Radial distribution functions

Various radial distribution functions can be computed. The total correlation function, T(r), is useful for direct comparison of simulated structures to neutron diffraction data, since the broadening function required to account for the experimental neutron scattering length is symmetric and *r* independent, making the broadening relatively simple to implement. The resulting broadened distributions compare very well to experimental data. The quality of the simulation compared to a given experiment can readily be quantified by taking the mean square deviation across T(r), via

$$R_\chi = \left(\frac{\sum_i \left[T_{\exp}(r_i) - T_{sim}(r_i) \right]^2}{\sum_i T_{\exp}^2(r_i)} \right)^{1/2} .$$

b) Non-bridging oxygens, Q^n numbers, and coordination number

Three main defects in silica and related materials are non-bridging oxygens (nbo), 5 coordinated Si atoms (V-Si), and 3 coordinated oxygen atoms (III-O). (These defects are discussed in more detail in the next section on "Results for Silica.") The Q^n number characterizes the local number of nbo, defined as the number of nbo atoms bound to a given Si atom, *i.e.*, for a given Si atom with *y* nbo defects, $n = 4 - y$. Non-bridging oxygens are those that are bonded to only one Si atom. The distribution of Q^n is a particularly sensitive metric to determine the fidelity of a glass model.

c) Angular distribution and ring statistics

Another useful metric is the distribution of bond angles in the glass, which is related to the ring structure. In crystalline quartz, all Si–O–Si bonds make an angle of 109.5°, within Si 6-memebered rings. In a silicate glass, especially with glass forming elements like Na, the ring structure is broken and larger and smaller rings are formed. These larger rings have larger Si–O–Si bond angles. For example, Fig. 1 shows the average of all Si–O–Si bond angles in a 30:70 sodium silicate glass structure, averaged over the 300 K equilibration trajectory. The peak is at the expected angle ~150° for sodium silicate glass, with the large broadening typical for amorphous structures. Figure 2 shows the distribution of Si rings in the structure.
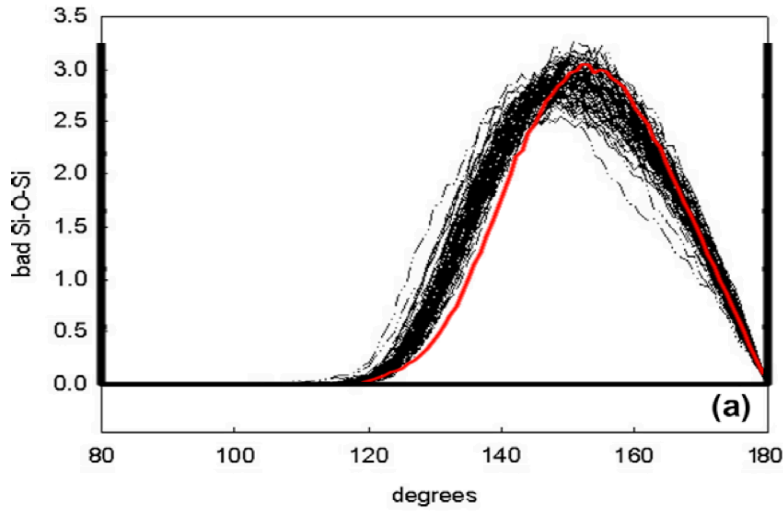
FIGURE 1. Si–O–Si bond angle distribution averaged over 50 equilibrated snapshots of the simulated E-glass 30:70 sodium silicate glass (thick red line), compared to an experimental ensemble of glass structures.[8]
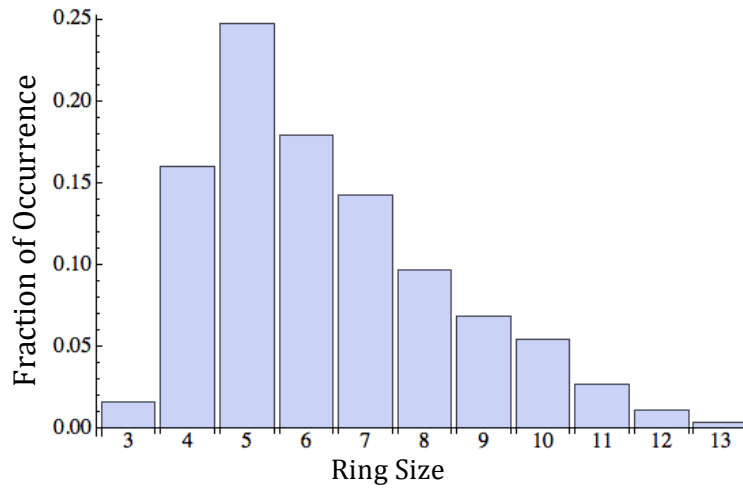
**FIGURE 2.** Distribution of Si ring sizes in the 30:70 sodium silicate glass model.

Electronic Structure

a) Electronic density of states (DOS)

The electronic density of states (DOS) is extracted using density functional theory (DFT) on snapshots of the atomic structure from the semi-empirical melt-quench simulations. Typically, system sizes on the order of 600-700 atoms are used, to give a good compromise between sample volume and tractability for calculation with DFT-PBE. Since the empirical potentials have some inaccuracies due to their approximate nature, the structures need to be relaxed within DFT before extracting the DOS. Generally, we perform the relaxation until all forces are below 0.05 eV/Å, using converged forces results (~700 eV typical plane-wave cutoff with the projector-augmented

wave method in the VASP code). For such large system sizes (and the amorphous nature of glass), using only the Γ point to sample the supercell Brillouin Zone is sufficient.

The purpose of using multiple snapshots is that the ergodicity principle equates averages in time from a MD simulations to averages in space. Thus, we use an ensemble average in time to effectively determine the average results over a larger sample volume than the supercell. As long as the supercell is large enough that boundary conditions to do not alter the distribution of local structure, this approach is valid. We generally test for finite-size effects before running the DFT DOS extraction. One issue with averaging the DOS over time is that arbitrary shifts in energy arise from each snapshot due to different occupation of band tail states (near the top of the nominal valence band maximum). These shifts need to be re-aligned so that the DOS from each snapshot can be averaged directly. We have automated this process by tracking the position of deeper semi-core states. For example, Fig. 3 shows the DOS from 30 snapshots of 30:70 sodium silicate glass (more details are presented in the Results sections below), where the relative energy scale shifts are apparent. The peaks between –15 and –25 eV are used to align all of the spectra. The result for the averaged DOS is shown below in the "Results for Sodium Silicate" section.
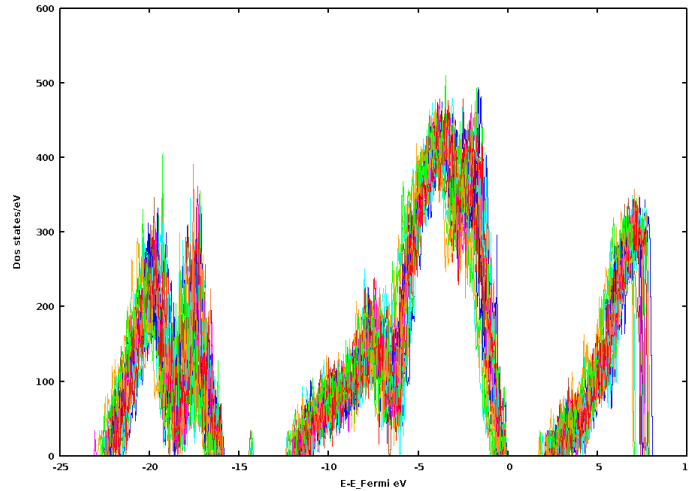
FIGURE 3. Electronic density of states of 30 snapshots of 30:70 sodium silicate glass containing 648 atoms after relaxation with DFT. The nominal VBM is set at 0.0 eV for each snapshot, but the variations of occupied gap states in each snapshot requires the energy scales to be individually shifted to align the "true" VBM.

b) Inverse participation ratio (IPR)

The quantitative localization of states is analyzed using the inverse participation ratio (IPR), which is a good measure of the spatial localization of a function. The IPR is defined as

$$I(\psi_n) = N \frac{\sum_{i=1}^{N} |\psi_n(\vec{r}_i)|^4}{\left[\sum_{i=1}^{N} |\psi_n(\vec{r}_i)|^2 \right]^2},$$

where ψ is a scalar function in 3D. A large value of IPR denotes a localized state (trap state), while a value near 1 denotes a completely delocalized (conduction) state. For our purposes, we

compute the IPR for each Kohn-Sham state (ψ) corresponding to energies around the band gap region. To compute all of the IPR values, a large number of partial charge density distributions must be generated, each of which is mapped onto a real-space grid whose spacing is dictated by the plane-wave cutoff. To speed up this large number of calculations, after convergence, we remap the total charge density onto a sparser grid using a 400 eV plane-wave cutoff. Figure 4 shows a range of ~200 calculated IPR, demonstrating no loss in fidelity by remapping to the sparser charge density grid. The data in Fig. 4 are illustrative.
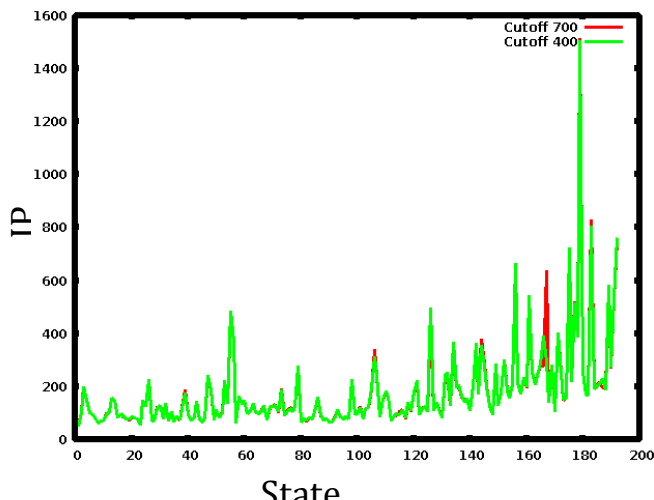

FIGURE 7. IPR values for a subset of energy states near the band gap from one snapshot of 30:70 sodium silicate glass. Red and green lines compare the results using charge densities mapped onto a grid corresponding to 700 eV and 400 eV plane-wave cutoffs, respectively.

Results for Silica [SiO$_2$]

Atomic Structure Generation

To generate atomic structural models of amorphous SiO$_2$ (silica) using a computational melt-quench procedure, we tested three semi-empirical potentials: the Tersoff potential, the Garofalini modified BMH 2-body potential, and the Garofalini modified BMH 3-body potential.[1] We implemented the modified BMH 2-body and 3-body potentials in the LAMMPS classical molecular dynamics code to perform the simulations. Previous work has applied the Tersoff potential to simulate the structure of silica glass, and our tests largely agree with that work: while the Tersoff potential yields a reasonable glass structure, it is somewhat over-structured based on comparison to the experimental structure factor [or pair correlation functions g(r)] measured with neutron diffraction. The Garofalini potentials are more physically-based and fitted over a wide set of glass materials. In general, when the 3-body terms are included they perform better than the Tersoff potential for predicting structure, and also predict a more accurate melting temperature. Figure 5 shows an illustration of the melt-quench glass generation process and a comparison of the g(R) obtained for SiO$_2$ using the 3-body Garofalini potential in both crystalline and glass form against experimental data.

---

[1] Garo 3-body potential
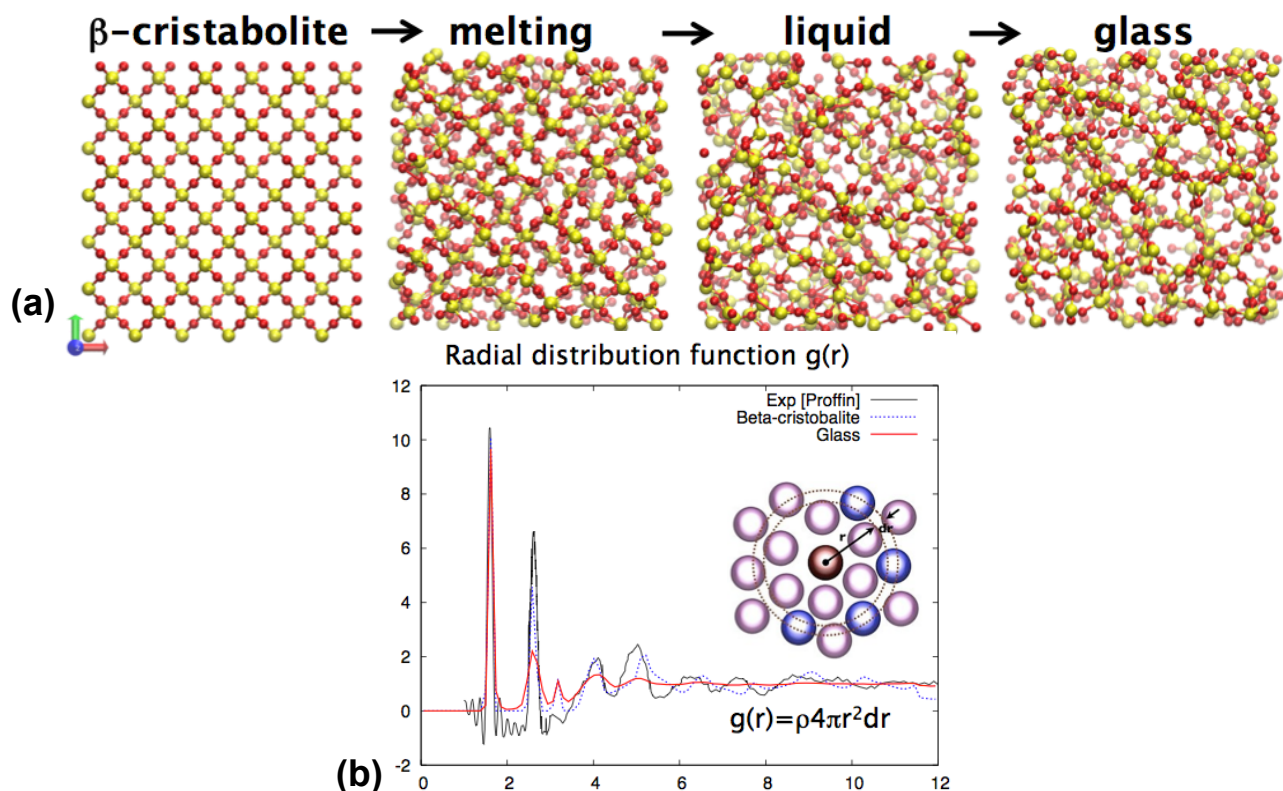
Figure 5. (a) Amorphous silica is constructed by computationally melting β-cristobolite (a crystalline form of SiO_2) and quenching the melt to room temperature using molecular dynamics. (b) Comparison of radial distribution function g(R) for the crystalline form, the melt-quenched structure, and experimental data for silica from neutron diffraction.

Parameters for 2-body and 3-body terms in the Garofalini potential are available (from personal communication with Prof. Garofalini, termed "E-glass" in this report) for quite a wide variety of glass compositions that include Si, O, Al, Ca, Na, H, B, and N atoms; potentials for other elements are available in more limited scope.
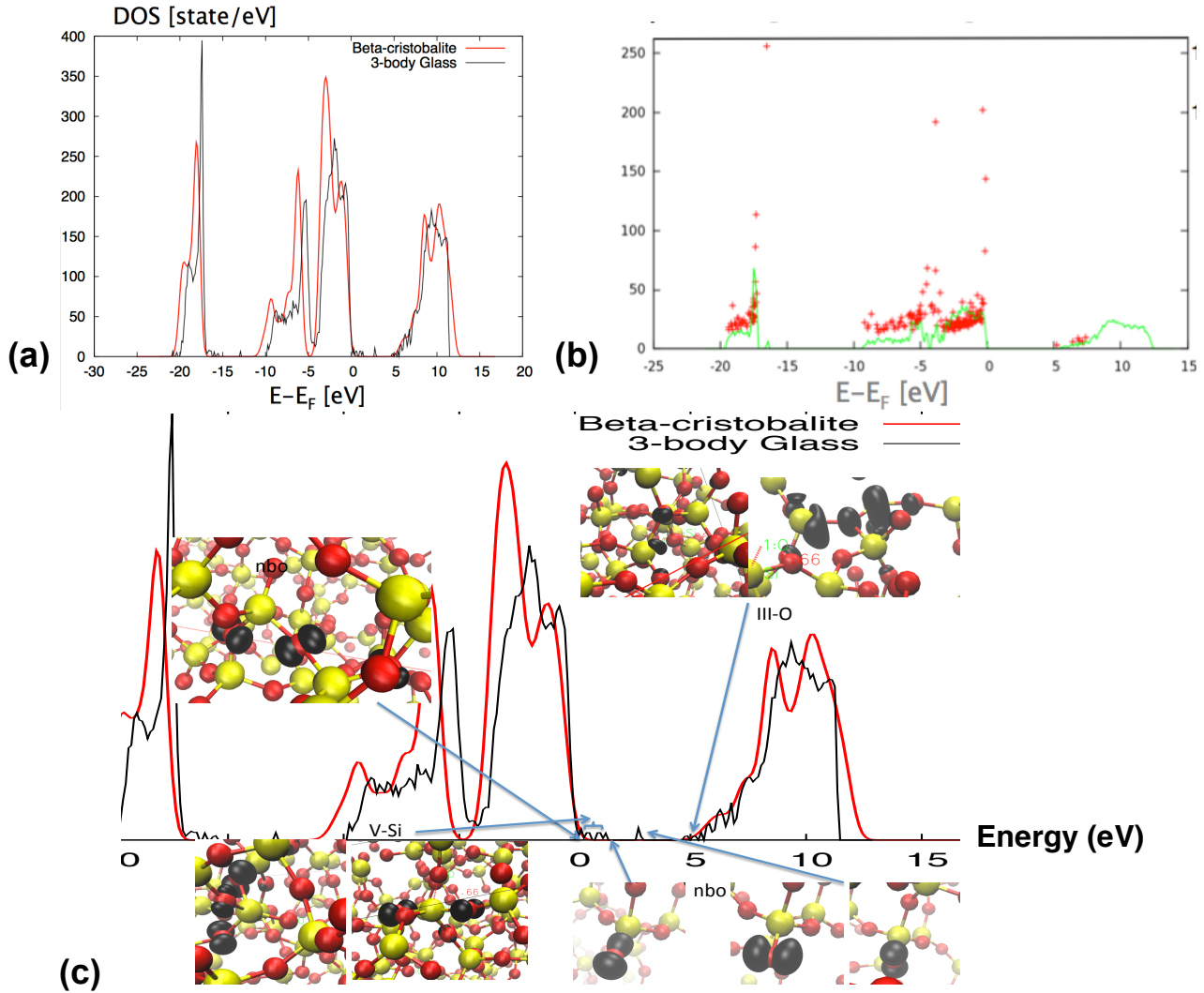
Electronic Structure

Snapshots of the atomic structure of the silica glass were taken periodically from the molecular dynamics simulation and used to calculate the electronic density of states (DOS) shown in Fig. 6. Gap states arising from structural defects are apparent, showing the Anderson localized states at the band edges and a larger mobility gap. The trapped localized states are involved in hopping-like polaronic transport. Structural analysis of the origins of the gap states shows that the states near the valence band maximum are derived from either non-bonded oxygen (nbo) defects or 5-coordinated Si (V-Si) defects. States near the conduction band edge are predominantly associated with 3-coordinated O (III-O) defects. In some structures, deep gap states associated with nbo also appear (see Fig. 6c).

Further quantitative analysis of the localization of states was performed by computing the inverse participation ratio (IPR) for each electronic state. Higher IPR values indicate more localization of a state, so a plot of IPR against the DOS demarcates the localized band tail region

against the delocalized band states. Figure 6b shows this analysis for the SiO_2 glass, where localized band tail states near the VBM are most apparent. The energy width of the band tail region is also an (inverse) measure of band edge conductivity in the material. For silica, we notice only a modest localized band tail of less than ~0.8 eV where the IPR values are large (Fig. 6b).

Figure 6. (a) Electronic density of states (DOS) of crystalline vs amorphous SiO_2, showing band edge and gap states appearing for the amorphous form. (b) IPR (red points) plotted again DOS (green line) for the amorphous structure, showing high degree of localization associated with gap and edge states. (c) Zoom-in of DOS, with isosurfaces of partial charge (in black) plotted for each edge or gap state associated with amorphous structure. The character of each state is labeled as nbo, V-Si, or III-O. (yellow = Si, red = O)

Results for Sodium Silicate [Na₂(SiO₂)ₙO]

The $Na_2(SiO_2)_nO$ [sodium silicate] system was chosen for comparison to silica (and also to compare different sodium compositions), since a body of experimental structural information exists for a range of Na compositions and also since it represents a glass system that has been studied for scintillators. While it is not a top-performing glass scintillator host, it will serve as a

good benchmark system and given its relation to silica, there is good confidence in the ability to accurately model its structure using the same potentials. In addition, the system is convenient for the study of the effects of local structural order, since Na in silica is a bond-breaking additive.

Structure Generation and Model Validation

We constructed validated atomistic models of sodium silicate glass using melt-quench-anneal simulations with semi-empirical potentials. The resulting structures were validated against available neutron diffraction data from the literature. The chosen test glass (sodium silicate) is formally composed of a mixture of Na_2O and SiO_2 fragments. We worked with compositions given by the ratio of $Na_2O:SiO_2$ of 1:2, 1:3, and 3:7. The initial structures are generally built starting from a crystalline form of SiO_2 (beta-crystabolite) and replacing random moieties of SiO_2 with Na_2O before melting. However, tests comprised of initially placing the appropriate stoichiometry of all atoms in a supercell randomly yielded identical results, and the initial conditions do not sensitively affect the resulting structures.

We used a 3-body modified-BMH potential provided by Prof. Garofalini (Rutgers) to generate the glass structures. Two sets of parameters were compared, as well as the results using a different potential from the literature due to Yuan and Cormack. Additional details of melt-quench parameters and procedure are given below, but for these comparisons several different parameters were tested, with little sensitivity. For example, quenches from 8000 to 300 K or 5000 to 300 K were used, with quench rates between 5 and 100 K/ps. Molecular dynamics time steps of 1 or 2 fs were used. Experimental densities of 2.4–2.5 g/cm^3 were used with boxes containing ~800–1500 atoms. (We desire to keep our atom count low enough to be able to run DFT-based electronic structure calculations on the same systems later.) The results of these tests are summarized in Fig. 7, which shows the total pair distribution function obtained from the revised Garofalini potential ("E-glass"), a previous version of the potential ("Melman 1991"), the "Cormack" potential, and neutron diffraction data from Wright. While the Yuan-Cormack potential agrees slightly better with the experimental data at short range, the Garofalini potentials match the mid-range order better. Tests with 1500-atom and 648-atom supercells showed that the cell size had little effect on the results.
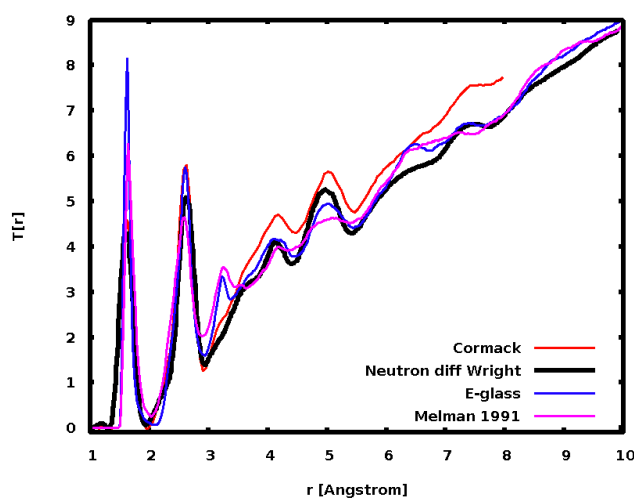
FIGURE 7. Total pair distribution function $T(r)$ for 3:7 ($Na_2O:SiO_2$) sodium silicate glass (768 total atoms) obtained from melt-quench with different potentials (thin colored lines), compared to experimental neutral diffraction data (thick black line).

Details of Glass Model Generation Procedure

The glass forming procedure starts with swapping out Si and O atoms for Na from a 4x4x4 β-cristobalite cell and setting the volume to correspond to the experimental density of 2.466 g/cm^3. Molecular dynamics are run using a time step of 1 fs and a Langevin thermostat. First, the structure is minimized at 0 K, and then the temperature is increased from 0 to 8000 K while the volume is scaled up by 16.7% to account for thermal expansion. After equilibrating at 8000 K, a snapshot is taken every 32,000 steps (32 ps) to seed an ensemble of glass structures. Each melt snapshot is quenched to 300 K over 80,000 steps (80ps) while rescaling the volume every 8000 steps, which is equivalent to a quench rate of ~10^{14} K/s. This quench rate is similar to that used for previous work in the literature and gives defect concentrations similar to experiment, although it is a fast quench. Finally, each quenched snapshot is equilibrated at 300 K for 80 ps, during which structural statistics are accumulated.

We focused our study on the 30:70 Na$_2$O-SiO$_2$ composition, to verify our potentials and glass forming methodology. We also compared to a 2001 study[2], which used only 90 atoms (compared to our 660) to simulate the glass and used a different variable charge BKS classical potential. We also compared our results to slower quench rates.

Potential Parameters

The potentials used in this study (referred to as "E-glass") are from a private communication with Prof. Stephen Garofalini of Rutgers University; the potential form, which includes 2- and 3-body terms, is a modified form of the BMH potential and is presented in a paper by Feuston and Garofalini.[3]

Fig. 8(a) shows that the radial distribution function (rdf) from the Melman paper compares well to the rdf from our simulation using the same parameters; the revised E-glass parameters give slightly different results, but also agree slightly better with experiment. We also verified excellent agreement of the Si–O–Si angular distribution, as shown in Fig. 8(b). Furthermore, the more sensitive metrics of Q^n distribution and fraction of non-bridging oxygen (nbo) atoms also agreed well, as shown in Table 1.
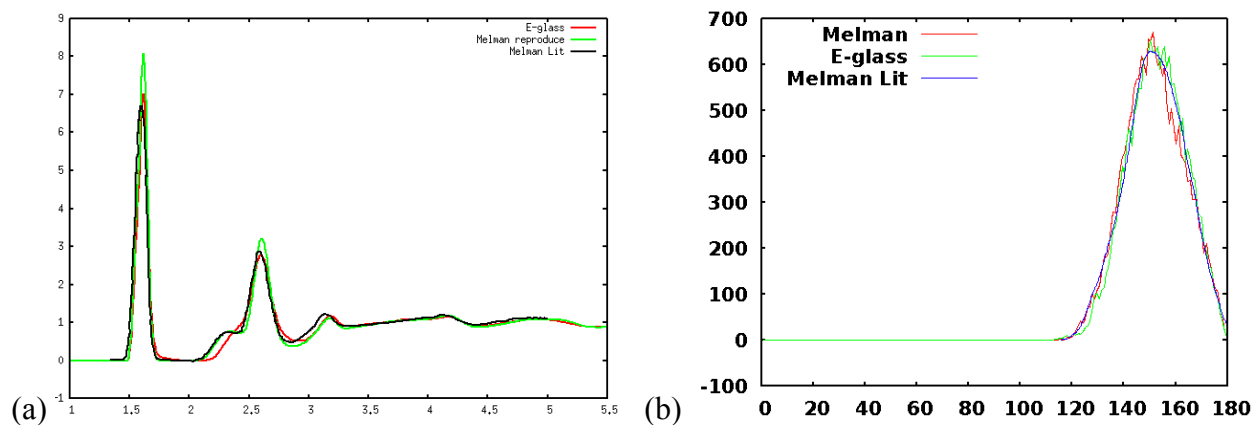
FIGURE 8. (a) Radial distribution function of sodium disilicate from simulations using revised E-glass parameters compared to the corrected parameters from Melman and Garofalini. (b) The angular distribution of Si–O–Si bonds in the same simulations.

[2] X. Yuan and A. N. Cormack, Journal of Non-Crystalline Solids 283, 69 (2001).
[3] B. P. Feuston and S. H. Garofalini, The Journal of Chemical Physics 89, 5818 (1988).

Q^n species % sodium disil.	Melman Literature	Melman	E-glass
Q^4	31.0	30.9	33
Q^3	44.6	42.7	41.4
Q^2	20.2	24.0	23.1
Q^1	4.1	2.36	2.5
Q^0	0	0	0
% nbo	38	38.75	37.7

TABLE 1. Validation of distribution of Q^n and fraction of nbo for sodium disilicate simulations from Fig. 1.

In Table 2 we show the $R\chi$ values comparing the quality of total correlation functions computed from simulations of 3:7 sodium silicate glass using the three different potentials (Cormack BKS, E-glass, and Melman), against to two different experimental data sets by Wright[4] and Johnson.[5] According to these results, the BKS potential performed slightly better than E-glass, however, we have chosen to use the E-glass potential, since it performs reasonably well and since the variable charge in the BKS potential will be difficult to use in multicomponent glasses moving forward. Figure 9 shows a representative T(r) comparison between simulation and experiment for the E-glass potential, used to compute the $R\chi$ values.

Potential	Wright	Johnson
BKS (Yuan-Cormack)	13.2 %	12.5 %
E-glass	18.9	18.4
Melman	20.6	19.8

TABLE 2. $R\chi$ values for 3:7 sodium silicate simulated structures generated with 3 different potentials (BKS, E-glass, Melman) compared against 2 different experimental neutron diffraction data sets (Wright, Johnson).
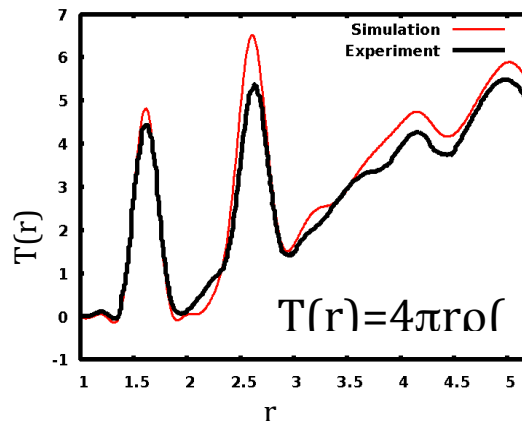
FIGURE 9. Comparison of broadened T(r) from "E-glass" simulation to Wright experimental data.

[4] A. C. Wright, Journal of Non-Crystalline Solids 159, 264 (1993).
[5] J. A. Johnson, C. E. Johnson, D. Holland, A. Mekki, P. Appleyard, and M. F. Thomas, Journal of Non-Crystalline Solids 246, 104 (1999).

In Table 3, we show the distribution of Q^n and the fraction of nbo in our model compared to experimental results. The experiments, however, were for a slightly different glass composition (22.5:77.5 Na_2O:SiO_2, compared to our 30:70). The simulated structure shows a smaller fraction of Q^3 compared to the experiment and a correspondingly larger fraction of Q^2. This is consistent with an increase in nbo, as seen in the table, and is somewhat expected for the larger ratio of Na to Si atoms in the simulated glass. Other simulated structures in the literature, for similar types of glasses, have shown comparable results of lower Q^3/higher Q^2 compared to experiment.[6,7]

	Experiment[8] (22.5:77.5)	Simulation (E-glass) (30:70)
% nbo	28 %	34.0 ± 0.4 %
% Q^4	37.2 %	37.4 ± 1.9 %
% Q^3	60.5	44.8 ± 3.5
% Q^2	2.3	15.6 ± 2.3
% Q^1	0	2.1 ± 1.1
% Q^0	0	0.09 ± 0.3

TABLE 3. Fraction of nbo and distribution of Q^n for our simulated 30:70 sodium silicate glass structure, compared to experimental glass with similar composition (22.5:77.5 sodium silicate).

We also studied the effect of quench rate on the obtained structure, over 4 orders of magnitude from 0.01 to 100 K/ps. The fastest quench rate (100 K/ps) resulted in obvious over-structuring of the glass, with sharper short-range peaks in the pair distribution function compared to experiment. Good agreement with experiment was achieved with the slower quench rates, with little difference between 0.01 and 0.1 K/ps. Thus, 0.1 K/ps seems like an optimal quench rate for structure generation.

Electronic Structure

To analyze the electronic properties and statistics in details, we sampled 30 random configurations ("snapshots") from the 30:70 sodium silicate melt at 8000 K. Each sample was quenched to 300 K, then relaxed to a local minimum at 0 K with density functional theory (using the PBE exchange-correlation functional) to extract the electronic states. Various detailed analyses of each snapshot were performed, but here we report mainly results averaged across all snapshots, to best describe a bulk volume of glass. The shaded blue curve in Fig. 3 shows the averaged electronic density of states (DOS), after aligning all of the individual energy scales to match the deep states near –20 eV.

The energy between the highest occupied defect state and the lowest unoccupied state is about 1.5 eV. However, this is not to be considered the band gap of the material, as these states are associated with defects within the mobility gap (in addition to the normal band gap

[6] M Pota, A Pedone, G Malavasi, C Durante, M Cocchi, and M C Menziani, Computational Materials Science 47, 739 (2010).
[7] J. Du and A. N. Cormack, Journal of Non-Crystalline Solids 351, 2263 (2005).
[8] F. Angeli, O. Villain, S. Schuller, S. Ispas, and T. Charpentier, Geochimica et Cosmochimica Acta 75, 2453 (2011).

underestimate by PBE). The defect states in the gap are localized to various degrees, which we quantify using the inverse participation ratio (IPR) metric, discussed later.

The first peak below the VBM in the DOS is primarily from localized non-bridging oxygen (NBO) defect states. For our 30:70 glass, this peak is larger than for tetrasilicate (20:80) glass in the literature, which is expected since the higher sodium content in our glass results in more NBO defects. In addition, the tetrasilicate glass has a distinct peak near the conduction band minimum (CBM), while the band tail near the CBM in our calculation is more spread out.

To analyze the spatial localization, and consequent trapping character, of each state near the band edges, the IPR is calculated from the projected partial charge density of each Kohn-Sham state ("bands"). A large value of IPR indicates a very localized state, while values near unity are completely delocalized conduction or mobility states. This analysis can help quantitatively distinguish the localized band tail states from the mobility edges. The IPRs of all the bands near the VBM are plotted as dots on top of the DOS in Fig. 10, which shows that localized defects extend at least 3 eV below the nominal VBM, with a general trend of more localized states toward higher energies. This bandwidth of the band tail states (~3 eV) is much larger than observed for silica (< 1 eV), indicative of much poorer band edge mobility for the sodium silicate glass compared to silica. These results are in agreement with experiments that have demonstrated some scintillation in SiO_2:Ce, but essentially no scintillation from sodium silicate-based devices. (NOTE: The states near the bottom of the CBM are in general more delocalized and not included in Fig. 10 for clarity.)
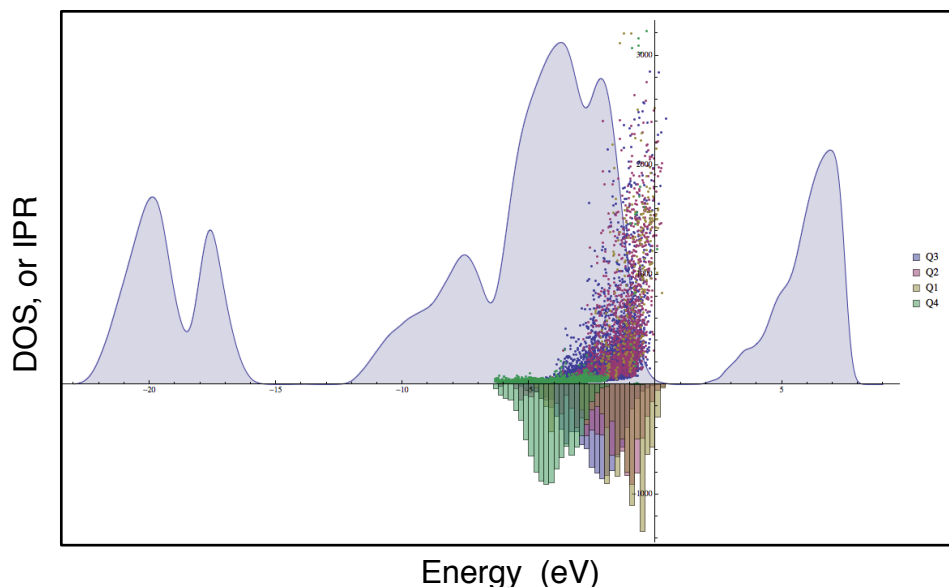

FIGURE 10. Averaged electronic DOS over 30 snapshots of 3:7 sodium silicate glass (blue shaded curve). The IPR of each state near the VBM is plotted with colored dots, coded by the Q^n-number character of the state (color given by key at right). Histograms of all the IPR values are plotted below the axis.

The character of each state can be determined by calculating its projection onto atomic orbitals. This also allows us to correlate each state with a structural feature, as follows. The top of the valence band is predominantly O-$2p$ in character, and the localized defects near the VBM are often associated with non-bridging oxygen atoms. We characterize an NBO atom by the Q^n value of the Si to which it is bonded. In this way, we have color coded the IPR values plotted in Fig.

10, associating each state with a Q^n structural characteristic: Q^4 is green, Q^3 is blue, Q^2 is pink, Q^1 is yellow. Qualitatively, we observe that as the Q^n number decreases, the localization and energy of the defect increases. This is more easily seen in the histograms of the IPR values, as a function of energy, plotted below the *x*-axis in Fig. 10. The yellow Q^1 distribution is seen to be peaked highest in energy, followed by the pink Q^2, the blue Q^3, and finally the green Q^4. The distributions are not uniform and also overlap, indicating the variations of this general trend.

For comparison, an example analysis of a single snapshot is shown in Fig. 11. Here, we see the DOS near the VBM for a single snapshot (black line), along with various partial DOS (colored lines). The IPR values are plotted as brown symbols, showing the general trend of increased localization toward the top of the valence band, with significant localization starting around 1.5–2.0 eV below the nominal VBM. The red symbols plot the predominant Q^n value of each state (1 to 4). In this particular snapshot, we see that Q^1 states dominate the band edge, followed by a mixture of Q^2 and Q^3, and higher values of Q^n characterizing the delocalized states deeper in the DOS. The general trend is similar to the total result in Fig. 10.
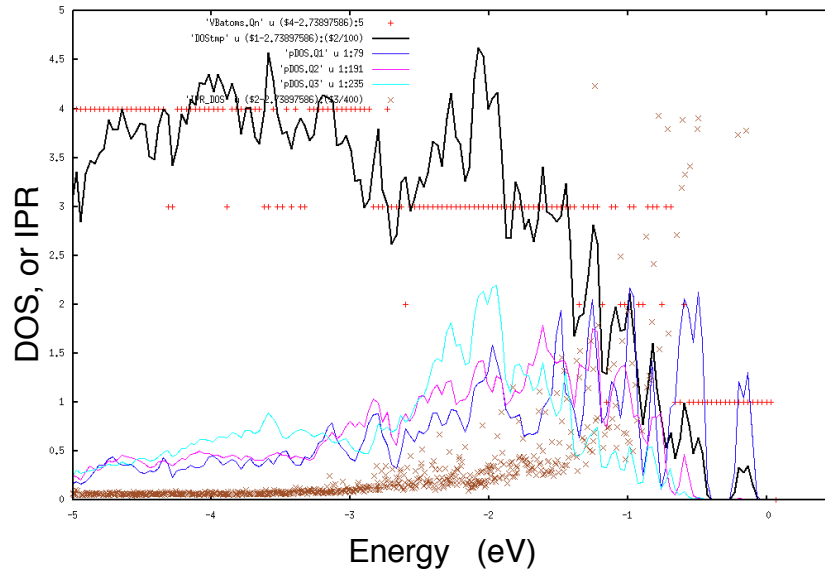
FIGURE 11. Total (black line) and partial (colored lines) DOS from a single snapshot of 3:7 sodium silicate glass. Brown symbols plot the IPR of each state, similarly to Fig. 3, with the predominant Q^n character of each state plotted as red symbols.

Finally, we can analyze the defect states directly in terms of localization by re-plotting the distribution of states on an IPR (localization) scale, as in Fig. 12, which shows histograms of each state within 6 eV of the Fermi level associated with a given Q^n value over IPR. Here, we see clearly that states are more localized when associated with Q^1 or Q^2 oxygen atoms compared to Q^3 or Q^4. The spread of the IPR values associated with Q^4 oxygens is very narrow, at low values that indicate very delocalized states. On the other hand, states associated with Q^1 or Q^2 oxygens have a wide spread and cover very large (very localized) IPR values. The distribution for Q^3 is in between. These results are integrated over all the states, irrespective of energy, so clearly show the correlation of localization of states and Q^n structural character. The distribution in Fig. 10 indicates their locations and spreads as a function of energy.
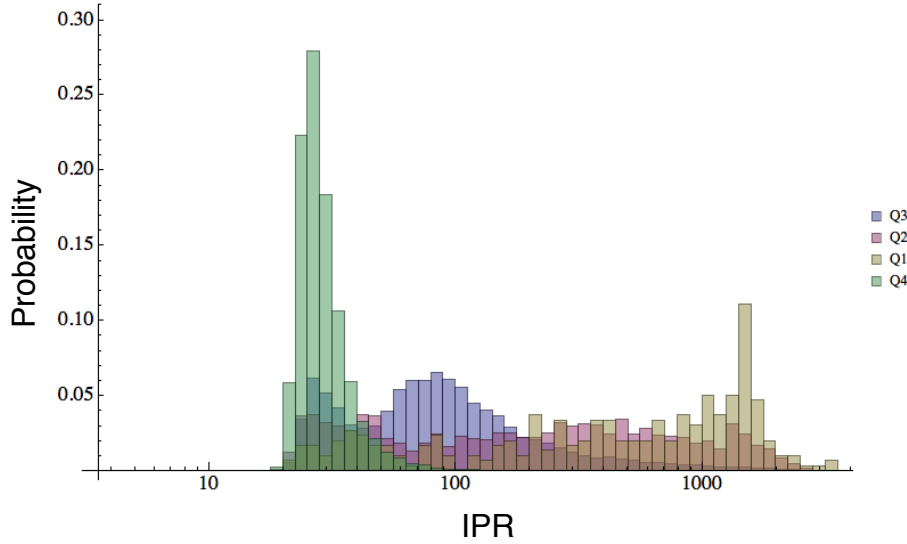
FIGURE 12. Histogram of IPR values, separated by Q^n, for 3:7 sodium silicate glass.

Summary

In summary, we calculated the atomic and electronic structure of silica and sodium silicate glasses (focused mostly on the 30:70 composition for the latter). Our analysis gives a detailed view of the localization and character of states near the band edges, beyond what has been previously done.

For silica, we find gap states near the valence band maximum derived from either non-bonded oxygen (nbo) defects or 5-coordinated Si (V-Si) defects. States near the conduction band edge are predominantly associated with 3-coordinated O (III-O) defects. In some structures, deep gap states associated with nbo also appear. The bandwidth of localized band tail states is less than 1 eV, indicative of modest hopping transport mobility at the band edge.

For sodium silicate, we find that nbo introduced by the incorporation of alkali ions (Na) into silicate glass can create many highly localized hole traps near the VBM, with the propensity for trapping correlated with increased local structural perturbation characterized by increased numbers of nbo (lower Q^n number). Increased concentrations of Na promote additional nbo and stronger carrier trapping near the band edge. This is manifested in higher concentration of low Q^n number structures associated with strong trapping/localization of states (large IPR), as well as a wider bandwidth ~3 eV of localized band tail states, indicative of poorer band edge mobility.

These results form a strong basis for continued work comparing additional glass compositions to vector toward understanding of favorable atomic structural features for improved carrier transport in glass hosts for scintillators.